1. Citation: Zongying Lai#, Xiaobo Qu#*, Yunsong Liu, Di Guo, Jing Ye, Zhifang Zhan, Zhong Chen*. Image reconstruction of compressed sensing MRI using graph-based redundant wavelet transform, Medical Image Analysis, DOI: 10.1016/j.media.2015.05.012, 2015. (# denotes co-first authorship, * denotes the corresponding author) (SCI, JCR 1, 3-Year IF 4.09).
2. Published version is available at http://dx.doi.org/10.1016/j.media.2015.05.012

Image Reconstruction of Compressed Sensing MRI Using Graph-based Redundant Wavelet Transform

Zongying Lai[1#], Xiaobo Qu[1#,*], Yunsong Liu[1], Di Guo[2], Jing Ye[1], Zhifang Zhan[1], Zhong Chen[1,*]

[1]Departments of Electronic Science and Communication Engineering, Fujian Provincial Key Laboratory of Plasma and Magnetic Resonance, Xiamen University, Xiamen 361005, China.

[2]School of Computer and Information Engineering, Xiamen University of Technology, Xiamen 361024, China.

# denotes co-first authorship

* denotes corresponding authors: quxiaobo@xmu.edu.cn; chenz@xmu.edu.cn

Abstract: Compressed sensing magnetic resonance imaging has shown great abilities to accelerate the magnetic resonance imaging if an image can be sparsely represented. How to sparsify the image seriously affects the reconstruction quality of images. In the present study, a graph-based redundant wavelet transform is introduced to sparsely represent magnetic resonance images in iterative image reconstructions. Using the l_1 norm regularized formulation of the problem solved by an alternating-direction minimization with continuation algorithm, experimental results demonstrate that the proposed method outperforms several state-of-the-art reconstruction methods in removing artifacts, and achieves lower reconstruction errors on the tested datasets.

Keywords: Compressed sensing, graph, wavelet, MRI, image reconstruction

Highlights

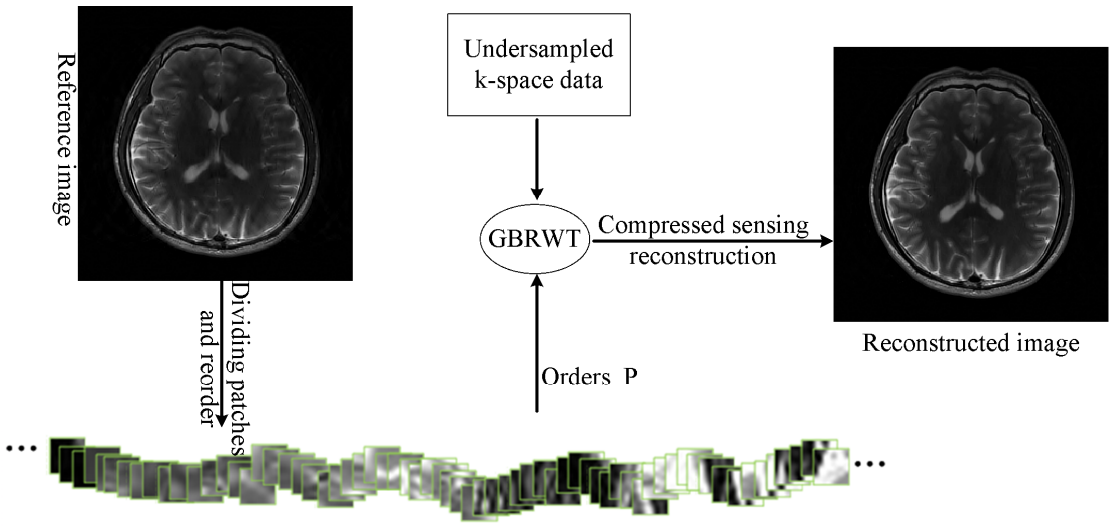

- A graph-based redundant wavelet transform (GBRWT) to sparsely represent MR images is proposed.
- GBRWT-based undersampled magnetic resonance image reconstruction method is proposed.
- Simulation results with added noise demonstrate a superior de-noising ability of the proposed method.
- Simulation results on *in vivo* data demonstrate that the proposed method achieves lower reconstruction error and higher visual quality than several state-of-the-art CS-MRI methods.

1. Introduction

Magnetic resonance imaging (MRI) is widely used in medical diagnoses because of its high resolution and noninvasiveness. However, physical conditions, e.g., gradient amplitude and slew-rate, and physiological conditions such as nerve stimulation, limit data acquisition speeds. Many researchers focus on accelerating MRI (Akcakaya et al., 2012; Chang and Ji, 2010; Chen et al., 2010; Jim and Zhi-Pei, 2001; Singh et al., 2011; Xiuquan et al., 2003). Compressed sensing MRI (CS-MRI) has shown to be promising to accelerate data acquisition by collecting fewer data than those required by Nyquist sampling theorem (Jacob, 2009; Weller et al., 2013; Ying and Ji, 2011). The CS can be further combined with parallel imaging to achieve higher acceleration factors (Huang et al., 2012; Weller et al., 2011). In general, three requirements exist in a successful CS application: sparse representation (Wang et al., 2014; Zhang et al., 2012), incoherent undersampling artifacts (Greiser and von Kienlin, 2003; Tsai and Nishimura, 2000), and an effective nonlinear reconstruction algorithm (Aelterman et al., 2011; Lustig et al., 2008; Majumdar and Ward, 2011, 2012; Majumdar et al., 2013; Yue et al., 2012).

In CS-MRI, finding an optimally sparse representation for magnetic resonance (MR) images is important because the reconstruction error is usually lower if the image representation is sparser (Qu et al., 2012; Qu et al., 2014; Qu et al., 2010; Ravishankar and Bresler, 2011). Conventional transforms, e.g., discrete cosine transform, total variation, wavelet transform, have been used to sparsely represent MR images in (Chaari et al., 2011; Khalidov et al., 2011). These methods represent an image sparsely by using predefined bases, which exhibit no difference among images. The image reconstruction may become unsatisfactory when the data are highly undersampled because of the insufficiently sparse representations (Qu et al., 2012; Ravishankar and Bresler, 2011).

Recently, patch-based methods have attracted considerable interest in CS-MRI because adaptively sparse representations can be trained with easy manipulations on patches (Akcakaya et al., 2011; Akcakaya et al., 2014; Maggioni et al., 2013; Ning et al., 2013; Qu et al., 2012; Qu et al., 2014; Ravishankar and Bresler, 2011; Wang and Ying, 2014; Yue et al.,

2014). For example, the geometric edge of a patch has been applied to train the adaptively sparse representations (Ning et al., 2013; Qu et al., 2012). Assuming that image patches are linear combinations of element patches, Aharon *et al.* have used K-SVD to train a patch-based dictionary (Aharon et al., 2006; Ravishankar and Bresler, 2011). Both methods significantly improve the image reconstruction over the predefined basis method (Ning et al., 2013; Qu et al., 2012; Ravishankar and Bresler, 2011). However, these methods sparsely represent each patch separately and neither of them considers the relationship, e.g., differences, among patches in the whole image. This relationship offers us an opportunity to take it into account to further remove artifacts in CS-MRI.

Recently, a graph is formed by viewing image patches as vertices and their differences as edges, and a shortest path on the graph is found to minimize the total difference of all image patches (Ram et al., 2011, 2012). This graph enables us to produce a smoother signal if a proper shortest path can be estimated. In this article, we introduce this graph-based transform into CS-MRI aiming at removing artifacts introduced by the k-space undersampling. Since smoother signals usually lead to sparser representation when wavelet coefficients are applied, the introduced transform is also called graph-based redundant wavelet transform (GBRWT) because it combines graph and redundant wavelets.

In the present study, we assume that a proper reference image is available in CS-MRI. All patches are reordered according to a short path on the graph, and a sparse representation is achieved by applying redundant wavelets to the smooth signal organized by traveling along this short path. Then, GBRWT is incorporated into an l_1-norm-based iterative MR image reconstruction.

The remainder of this article is organized as follows: Section 2 will present the implementation of GBRWT in MR images and the graph-based reconstruction model in CS-MRI. Main results on realistic MR imaging data will be given in sections 3. Discussions are presented in section 4. Finally, section 5 concludes this work and points out the future work.

2. Methodology

2.1. Conventional CS-MRI

Undersampled k-space data from an MR imaging scanner can be denoted by

$$\mathbf{y} = \mathbf{F}_{\mathrm{U}}\mathbf{x} + \boldsymbol{\varepsilon}, \tag{1}$$

where $\mathbf{x}$ is the discrete image to be reconstructed; $\mathbf{y} \in \mathbb{C}^M$ is the acquired k-space data; $\boldsymbol{\varepsilon} \in \mathbb{C}^M$ denote noises; and $\mathbf{F}_{\mathrm{U}} = \mathbf{U}\mathbf{F} \in \mathbb{C}^{M \times N}$ is the undersampling and Fourier transform, and directly relies on the undersampling scheme. An image is reconstructed by enforcing the sparsity of the image according to

$$\arg\min_{\mathbf{x}} \left\{ \left\| \boldsymbol{\Psi}^H \mathbf{x} \right\|_1 + \frac{\lambda}{2} \left\| \mathbf{y} - \mathbf{F}_{\mathrm{U}}\mathbf{x} \right\|_2^2 \right\}, \tag{2}$$

where $\boldsymbol{\Psi}^H$ transforms image $\mathbf{x}$ from spatial domain to sparse coefficients; $\|\cdot\|_1$ stands for the l_1 norm, which promotes the coefficients sparsity; $\|\cdot\|_2$ is l_2 norm which enforces data fidelity between reconstructed image and undersampled measurements; and λ controls the tradeoff between the sparsity and data fidelities.

Compared with traditional sparsifying transform, e.g., wavelets, which use predefined bases or dictionaries to sparse represent images, adaptive sparsifying transforms are tailored for a given image. As mentioned above, the geometric direction of each patch can be used to improve edge reconstructions (Ning et al., 2013; Qu et al., 2012), and K-SVD trains a dictionary to sparsely represent all patches (Ravishankar and Bresler, 2011). These methods have shown their unique properties in image reconstruction. But they do not consider the relationship, e.g., differences, among patches in the whole image. This relationship may help us to further remove artifacts in CS-MRI. Since wavelet transform can lead to sparser representations for smoother signals, we turn to produce smooth signals by incorporating prior knowledge of patch relationships. In the following text, a graph structure of image patches is constructed to provide adaptive sparse representations of a smooth signal in CS-MRI.

2.2. GBRWT-based CS-MRI

2.2.1. Graph based redundant wavelet transform

The wavelet transform provides sparse representations for piecewise smooth signals. However, if the signal does not satisfy this property, it may be suboptimal to apply wavelets to sparsify signals. This limitation encourages us to construct a new transform, which can adaptively make non-regular signals smoother first. For a weighted graph, where vertices denote signal points and edges denote differences of signal points, a shortest path that visits vertices will produce a smooth signal. If image pixels can be reorganized to be smoother according to a graph, sparser representations will be achieved by employing the wavelet transform.

Patch-based graph

Consider an image with size $\sqrt{N} \times \sqrt{N}$ denoted as $\mathbf{x} \in \mathbb{C}^{N \times 1}$. A weighted graph (Skiena, 2008) can be formed by assigning image pixels to be vertices, which are connected by edges indicating pixel differences. By finding a shortest path, which supplies new orders of pixels and will be illustrated below, a smoother signal will be produced if image pixels are permuted following the path. Therefore, wavelets can provide sparse representations of reordered pixels, although original pixels are non-smooth.

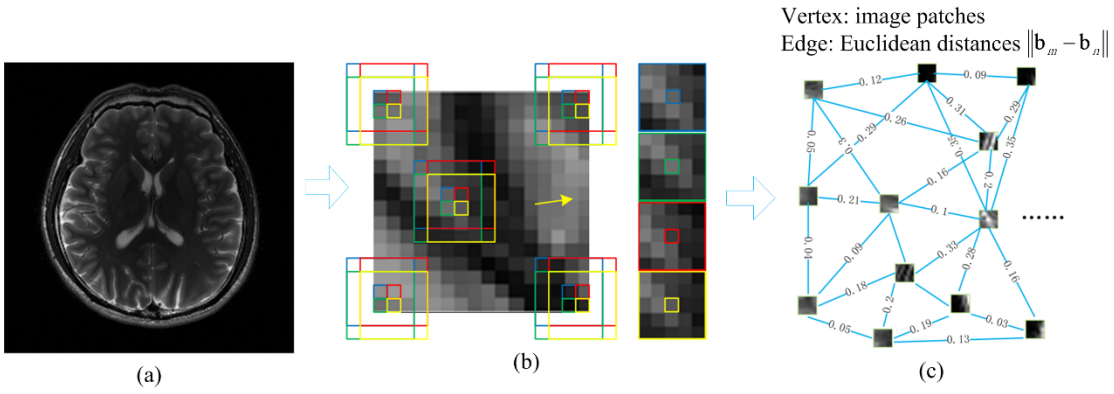

Fig. 1 Illustrative weighted graph of an MR image. (a) an MR image; (b) the process of dividing an image to patches; (c) a weighted graph. Vertices are image patches in B, and the weight denotes the Euclidean distance between patches. Note that these distances are used to explanatorily express distances but not real values.

A ground-truth-reference image to extract the path information exactly is unavailable in CS-MRI since k-space data are undersampled. Pixels are usually contaminated by noises and aliasing artifacts. Thus, measuring the similarity of pixels is impractical. Under the assumption that the distance between two pixels can be estimated by the distance between two patches whose centers are these two pixels, a graph (Fig. 1(c)) which is expected to be insensitive to noises and artifacts will be generated instead. At location (i, j), a vertex of the graph is a patch centered at (i, j). A patch with size $\sqrt{\rho}\times\sqrt{\rho}$ is denoted as $\mathbf{b}_m \in \mathbb{R}^{\rho\times 1}$ in the amplitude image. The distance $w_{m,n}$ between vertices is measured by

$$w_{m,n} = w(\mathbf{b}_m, \mathbf{b}_n) = \left\|\mathbf{b}_m - \mathbf{b}_n\right\|, \tag{3}$$

where $w_{m,n}$ indicates the intensity based similarity between m^{th} and n^{th} patches and a smaller $w_{m,n}$ implies less differences (Ram et al., 2011, 2012).

Pixels are reordered to be smooth by patch reordering. Patches are divided with overlaps and periodical boundary conditions (Fig. 1(b)). Correspondingly, each pixel is the center of one patch with the same overlapping factor. The slide distance between two neighboring patches is set to be $l = 1$. The overlapping factor is defined as: $c = \rho / l^2$ (Qu et al., 2012), where ρ is the aforementioned patch size. The overlapping strategy allows fast computations in reconstruction algorithm which will be explained in section *2.2.2.*

Finding the permutation

Minimum-cost patch orders that visit all the vertices exactly once imply a permutation of image pixels to be smoother when they are applied to a corrupted image. They are actually obtained by finding the 'shortest possible path' of the patch-graph. This finding is normally denoted as travelling salesman problem and is most notorious NP-hard problem, which is computation exhaustive. Ram *et al.* proposed a simplified algorithm to attain an approximate solution (Cormen et al., 2001; Ram et al., 2011, 2012, 2013), which is listed in Algorithm 1. We take the algorithm directly to pull through this problem.

To verify the sparsifying capability of GBRWT, we perform the same redundant wavelet

transform on pixels with the original order and new orders obtained with the shortest path. The decay of coefficients shown in Fig. 2 demonstrates that coefficients of new orders decrease much faster than those of the original order. Therefore, the graph-based transform leads to sparser representations by reordering signals than the wavelet transform that applies to signals of the original order.

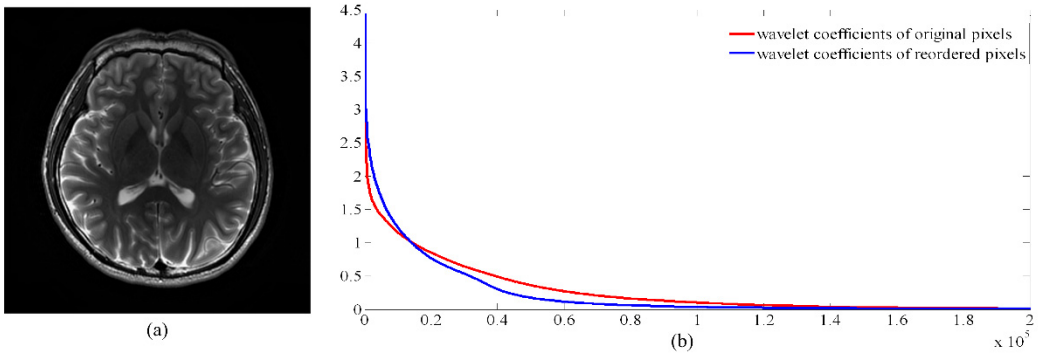

Fig. 2 Decay of wavelet coefficients. (a) an MR image size of 256×256; (b) shows the decay of coefficients by performing redundant wavelets on original pixels and graph-based reordered pixels.

Implement GBRWT

Based on the smoothing process using trained orders, reordered pixels of an MR image (Fig. 3) are expected to be sparsely represented with a redundant 1D wavelet (Shensa, 1992). Here, high-pass and low-pass filters in wavelet transforms are with no decimators thus each wavelet subband have the same length with the original signal. Incorporating with the permuting process, we modify the wavelet transform by rearranging signals before filtering them at each decomposition level. Correspondingly, graphs are constructed for wavelet coefficients in each subband. The inverse wavelet transform is implemented from finest to coarsest levels.

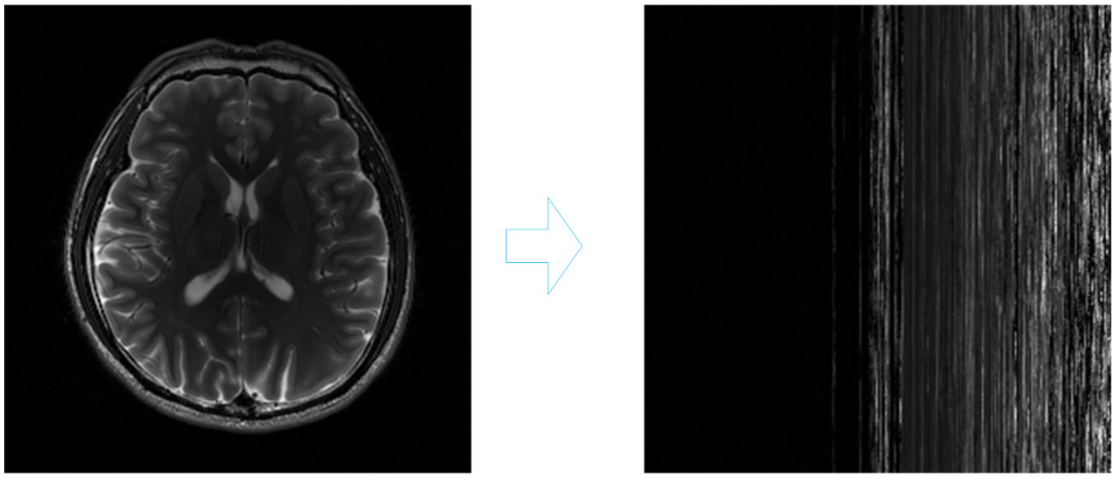

(a) image (b) reorderd pixels

Fig. 3 Reorder image pixels according to new orders. (a) the original image; (b) the reordered image pixels.

An image $\mathbf{x}$ is treated as a 1D signal in GBRWT, and the 1D wavelet is performed on this signal to achieve a sparse representation. Different patch-graphs are constructed in each wavelet subband, and different permutation matrices $\mathbf{p}_i^H$ can be obtained. In other words, new orders of coefficients in the i^{th} subband can be drawn from these patch graphs. For a g -level GBRWT, $\mathbf{P}^H = \{\mathbf{p}_1^H, \cdots, \mathbf{p}_g^H\}$ denotes permutation matrices in all decomposition levels. We use $\mathbf{\Psi}^H$ and $(\mathbf{P\Psi})^H$ to denote 1D wavelet transform and the reordered 1D wavelet transform. Therefore, the implementation of GBRWT on the image $\mathbf{x}$ can be expressed as $(\mathbf{P\Psi})^H \mathbf{x}$. Instead of reordering image pixels, patches in the graph are permuted without increasing complexities. Hence, we have a $\rho \times N$ matrix that contains all N -column-stacked patches inside the image $\mathbf{x}$ with a maximum overlapping factor. Rows of the patch matrix can be seen as shifted versions of the image. We denote each version of image as $\mathbf{x}_j = \mathbf{R}_j^H \mathbf{x}$, where $\left\{\mathbf{R}_j^H\right\}_{j=1,\cdots\rho}$ represents the original order of the shifted version. The $\mathbf{R}_j$ satisfies $\mathbf{R}_j \mathbf{R}_j^H = \mathbf{I}$, which implies that each shifted version will be restored by placing pixels to its original place. Note that: 1) the middle row is occupied by image pixels

reshaped as a 1D signal; 2) other rows are occupied by $\rho-1$ shifted versions of the image; 3) ρ versions of the image can be reconstructed. These reconstructed images can be averaged to remove the redundancy.

2.2.2. Undersampling and reconstruction based on GBRWT

With the aforementioned GBRWT, shifted versions of the image are obtained with additional redundancy, and the reordering-and-decomposition is applied on shifted versions of the image. We make use of these shifted versions to improve the reconstruction accuracy without increasing the computation complexities. Therefore, the MRI reconstruction model is modified as

$$\arg\min_{\mathbf{x}}\left\{\sum_{j=1}^{\rho}\left\|(\mathbf{P\Psi})^{H}\mathbf{x}_{j}\right\|_{1}+\frac{\lambda}{2}\left\|\mathbf{y}-\mathbf{F}_{\mathbf{U}}\mathbf{x}\right\|_{2}^{2}\right\}, \tag{4}$$

where $\mathbf{x}_j=\mathbf{R}_j^H\mathbf{x}, j=1,\cdots,\rho$ denotes shifted versions of the image; $(\mathbf{P\Psi})^H$ denotes the reordering-and-decomposition procedure, which works on all shifted version images in the same way, or for convenience,

$$\arg\min_{\mathbf{x}}\left\{\sum_{j=1}^{\rho}\left\|(\mathbf{R}_{j}\mathbf{P\Psi})^{H}\mathbf{x}\right\|_{1}+\frac{\lambda}{2}\left\|\mathbf{y}-\mathbf{F}_{\mathbf{U}}\mathbf{x}\right\|_{2}^{2}\right\}, \tag{5}$$

which is over-relaxed with a variable $\alpha_j=(\mathbf{R}_j\mathbf{P\Psi})^H\mathbf{x}$ to become

$$\min_{x,\alpha_j}\sum_{j=1}^{\rho}\left(\left\|\boldsymbol{\alpha}_{j}\right\|_{1}+\frac{\beta}{2}\left\|\boldsymbol{\alpha}_{j}-(\mathbf{R}_{j}\mathbf{P\Psi})^{H}\mathbf{x}\right\|_{2}^{2}\right)+\frac{\lambda}{2}\left\|\mathbf{y}-\mathbf{F}_{\mathbf{U}}x\right\|_{2}^{2}. \tag{6}$$

When $\beta\to+\infty$, expression (6) approaches (5) (Daubechies et al., 2004; Junfeng et al., 2010). In the expression (6), β is fixed during each inner iterative loop and then is increased continually during each outer loop. The continuation strategy of β speeds up the convergence rate, and has been proved in (Junfeng et al., 2008). When β is fixed, expression (6) can be computed by two alternating steps:

1) Fix $\mathbf{x}$, $\boldsymbol{\alpha}_j$ is computed via soft-thresholding

$$\alpha_j = S((\mathbf{R}_j \mathbf{P}\boldsymbol{\Psi})^H \mathbf{x}, \frac{1}{\beta}). \tag{7}$$

2) Fix all $\boldsymbol{\alpha}_j \{j = 1, \cdots, \rho\}$ and compute

$$\min_{\mathbf{x}} \sum_{j=1}^{\rho} (\frac{\beta}{2} \left\| \alpha_j - (\mathbf{R}_j \mathbf{P}\boldsymbol{\Psi})^H \mathbf{x} \right\|_2^2) + \frac{\lambda}{2} \left\| \mathbf{y} - \mathbf{F}_{\mathbf{U}} \mathbf{x} \right\|_2^2. \tag{8}$$

The minimum is given by

$$\begin{aligned} &(\beta \sum_{j=1}^{\rho} \mathbf{R}_j \mathbf{P}\boldsymbol{\Psi}\boldsymbol{\Psi}^H \mathbf{P}^H \mathbf{R}_j^H + \lambda \mathbf{F}_{\mathbf{U}}^H \mathbf{F}_{\mathbf{U}}) \times \mathbf{x} \\ &= \beta \sum_{j=1}^{\rho} \mathbf{R}_j^H \boldsymbol{\Psi}^H \mathbf{P}^H \boldsymbol{\alpha}_j + \lambda \mathbf{F}_{\mathbf{U}}^H \mathbf{y}. \end{aligned} \tag{9}$$

The wavelet transform is chosen to be a tight frame, thus satisfying $\boldsymbol{\Psi}\boldsymbol{\Psi}^H = \mathbf{I}$. The reordering of pixels is a forward and backward process, thus satisfying $\mathbf{P}\mathbf{P}^H = \mathbf{I}$. When the image is divided to patches, each pixel appears with same frequencies. Consequently, $\mathbf{R}_j \mathbf{R}_j^H = \Lambda \mathbf{I}$ is satisfied. Meanwhile, $\mathbf{F}_{\mathbf{U}}^H \mathbf{F}_{\mathbf{U}}$ can be expressed as $\mathbf{F}^H \mathbf{U}^H \mathbf{U}\mathbf{F}$. Equation (9) becomes

$$\left(\beta \Lambda \mathbf{I} + \lambda \mathbf{F}^H \mathbf{U}^H \mathbf{U}\mathbf{F}\right) \mathbf{x} = \beta \mathbf{s}_\alpha + \lambda \mathbf{F}_{\mathbf{U}}^H \mathbf{y}, \tag{10}$$

$$\mathbf{s}_\alpha = \sum_{j=1}^{\rho} \mathbf{R}_j \boldsymbol{\Psi} \boldsymbol{\alpha}_j. \tag{11}$$

Since $\beta \Lambda \mathbf{I} = \beta \Lambda \mathbf{F}^H \mathbf{F} = \mathbf{F}^H \beta \Lambda \mathbf{F}$, Eq.(10) is further derived as

$$\mathbf{F}^H \left(\beta \Lambda + \lambda \mathbf{U}^H \mathbf{U}\right) \mathbf{F}\mathbf{x} = \beta \mathbf{s}_\alpha + \lambda \mathbf{F}_{\mathbf{U}}^H \mathbf{y}, \tag{12}$$

leading to

$$\mathbf{x} = \mathbf{F}^H (\beta \Lambda + \lambda \mathbf{U}^H \mathbf{U})^{-1} (\beta \mathbf{F}\mathbf{s}_\alpha + \lambda \mathbf{U}^H \mathbf{y}). \tag{13}$$

Therefore, the solution $\mathbf{x}$ can be obtained with fast Fourier transform and entry multiplication on vectors. However, if pixels appear with different frequency, $\mathbf{R}_j \mathbf{R}_j^H = \Lambda \mathbf{I}$ will be a diagonal matrix with different values of diagonal entries. Then,

$(\beta\sum_{j=1}^{\rho}\mathbf{R}_j\mathbf{P}\Psi\Psi^H\mathbf{P}^H\mathbf{R}_j^H+\lambda\mathbf{F}_{\mathrm{U}}^H\mathbf{F}_{\mathrm{U}})$ cannot be diagonalized, and we must solve Eq. (9) with the conjugate gradient algorithm, which will be time consuming. The proposed GBRWT-based MRI reconstruction is shown in Algorithm 2.

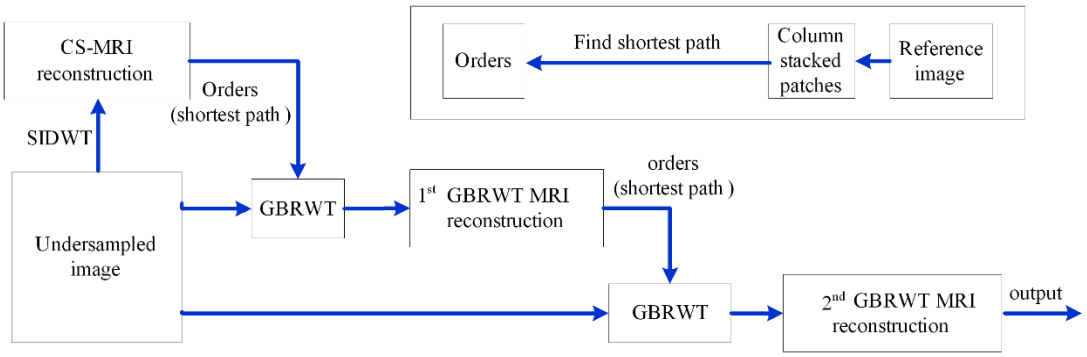

Fig. 4 Flowchart of GBRWT-based MRI reconstruction. The top right block diagram indicates the flow chart to find the shortest path in patch-graphs to find new orders.

We use the reconstructed image from conventional CS-MRI as the reference image to construct the graph and train new orders to permute pixels as shown in the flow chart (Fig. 4) to reconstruct MR images. A shift invariant discrete wavelet transform (SIDWT) (Baraniuk et al., 2011) is utilized to sparsely represent MR images in conventional CS-MRI. The reason of choosing SIDWT lies in that SIDWT can mitigate blocky artifacts introduced by orthogonal wavelet transform (Baker et al., 2011). Simulation results show that optimizing the graph using the first iteration reconstructed image can further improve the result, which is consistent to the observation in (Qu et al., 2012). Therefore, the GBRWT is conducted twice in the flow chart.

3. Results

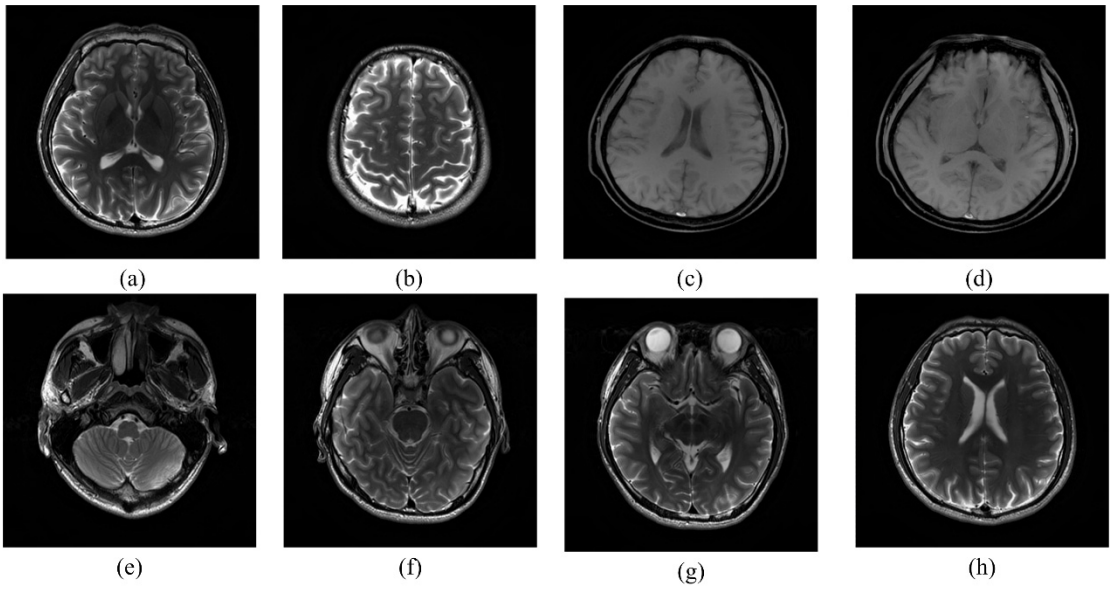

Fig. 5 Gold standard images used in the experiment. Images in the top row are used for Cartesian sampling and bottom row mainly for 2D undersampling.

To evaluate the performance of the presented method, we use 3 datasets in experiments. All k-space data are acquired on real MRI scanners. Dataset 1 (Fig. 5(a-b, e-h))are acquired from a healthy volunteer at a 3T Simens Trio Tim MRI scanner using the T2-weighted turo spin echo sequence (TR/TE = 6100/99 ms, FOV= 220×220 mm, slice thickness=3 mm). Dataset 2 (Fig. 5(c-d)) are acquired from another healthy volunteer at a 1.5T Philips MRI scanner with fast field echo sequence (TR/TE = 1700/390 ms, FOV= 230×230 mm, slice thickness=5 mm). Dataset 3 (Fig. 10(a)) are acquired from Simens MRI scanner using a turbo spin echo sequence (TR/TE=2000/9.7ms, FOV=230×187 mm, slice thickness=5mm).These data are done with SENSE reconstruction with a reduction factor 1 to compose full k-space of gold standard images, which will be used for emulating the single channel MRI. These gold standard images are shown in Figs. 5 and 10. The signal-to-noise ratio (SNR) is defined as

$$SNR = 10\log 10(u/\delta)\,, \tag{14}$$

where u is the mean of image density and δ is the standard deviation of the noise extracted from the image background. The SNR is measured on the magnitude of the image.

To demonstrate the efficiency of the proposed method persuasively, we employ the relative l_2 norm error (RLNE) to measure reconstruction errors. The RLNE is defined as

$$e(\hat{\mathbf{x}}) = \frac{\left\|\hat{\mathbf{x}} - \tilde{\mathbf{x}}\right\|}{\left\|\tilde{\mathbf{x}}\right\|}, \tag{15}$$

where $\hat{\mathbf{x}}$ is the reconstructed image and $\tilde{\mathbf{x}}$ denotes the full sampled data. A smaller RLNE implies higher consistencies between reconstructed and full sampled images.

Meanwhile, structure similarity index measure (SSIM) (Zhou et al., 2004) is introduced as a metric in this article. The SSIM is a widely used image quality assessment when a reference is available. We have full sampled images as references in this work. The SSIM on two corresponding local windows (one is from reference and the other to be assessed) is defined as

$$SSIM(a,b) = \frac{(2\mu_a\mu_b + C_1)(2\sigma_{ab} + C_2)}{(\mu_a^2 + \mu_b^2 + C_1)(\sigma_a^2 + \sigma_b^2 + C_2)}, \tag{16}$$

where μ_a is the mean intensity of a; μ_b the mean intensity of b; σ_a^2 the variance of a, and σ_b^2 the variance of b. Constants C_1 and C_2 are included to avoid instabilities when the denominator is very close to zero. For the quality assessment of the entire image, mean SSIM (MSSIM) is utilized instead. The MSSIM is defined as

$$MSSIM(A,B) = \frac{1}{M}\sum_{i=1}^{M}(A_i, B_i), \tag{17}$$

where A and B are the reference and the reconstructed image respectively; A_i and B_i are contents at i-th local window; M the number of local windows. Higher MSSIM values indicate stronger detail preservation in reconstruction.

Cartesian undersampling (Fig. 6) is chosen in our simulations because it is most widely used in practice. To investigate the performance of the GBRWT-based MRI reconstruction algorithm, we have compared GBRWT with SIDWT, which is a typical sparsifying transform, and patch-based directional wavelets (PBDW) (Qu et al., 2012), which is a recently proposed adaptive sparse representation of MR image patches. We also compared the proposed method with state-of-the-art methods, including K-SVD based dictionary learning MRI (DLMRI) (Ravishankar and Bresler, 2011), and wavelet tree-structured MRI (WaTMRI) (Chen and

Huang, 2014) in Section 4.3. Default parameters of these methods are used in image reconstructions.

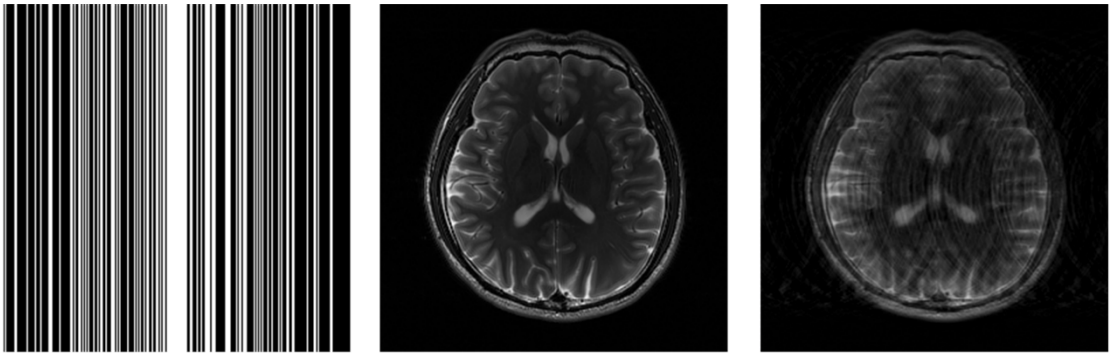

Fig. 6 Undersampling artifacts. (a) sampling pattern with undersampling rate 35%; (b) the full sampled image; (c) image with undersampling artifacts with zero-filling the k-space.

Typical settings of the proposed GBRWT-based MRI reconstruction method are: patch size 4×4 with a overlapping factor c=16 and 5 levels GBRWT decomposition for a 256×256 image. Daubechies wavelet with 4 decomposition levels is utilized for SIDWT. The PBDW-based reconstruction is carried out with its typical settings. Reconstructed images obtained from SIDWT-based CS-MRI are chosen as references for both PBDW and GBRWT. Optimizing on PBDW and GBRWT is conducted twice to gain performance improvements as shown in Fig. 4.

Simulation results show that the proposed method outperforms SIDWT and PBDW. Reconstruction errors in Fig. 7(f-h) indicate that the proposed method exhibits better intensity fidelities and edge-preserving capabilities. Furthermore, SIDWT and PBDW lead to obvious artifacts in the background of reconstructed images in Fig. 7(b) and (c). These artifacts are hardly observed in using GBRWT as shown in Fig. 7(d).

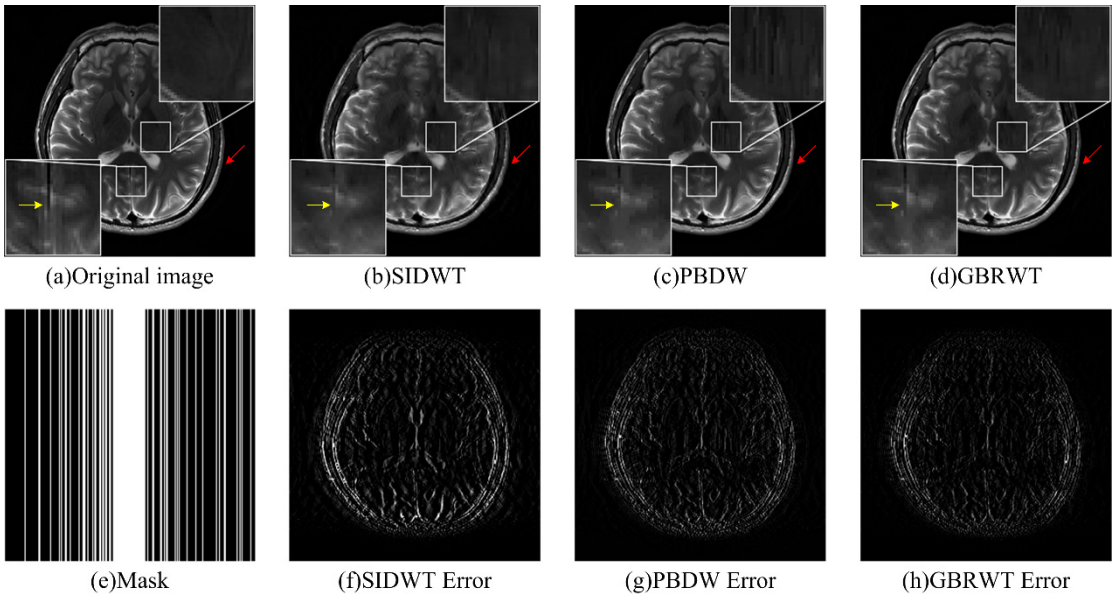

Fig. 7 Comparisons of SIDWT, PBDW and GBRWT-based reconstructions. (a) the full sampled image; (b-d) reconstructed images based on SIDWT, PBDW and GBRWT; (e) sampling pattern with undersampling rate 31%; (f-h) reconstructed errors (scaled 5x).

Table 1 shows RLNE, SNR and MSSIM for reconstructed images in Fig. 7. These criteria indicate that the proposed method recovers images most faithfully since it attains the highest MSSIM and SNR, as well as lowest RLNE.

Table 1 Evaluation criteria on image in Fig.7 using different methods.

Reconstructed images	SNR	MSSIM	RLNE
Fig. 7 (b)	14.88	0.8984	0.1431
Fig. 7 (c)	16.76	0.9168	0.1153
Fig. 7 (d)	**17.72**	**0.9376**	**0.1033**

4. Discussions

4.1. Different undersampling rates

The GBRWT leads to lower reconstruction errors than PBDW and SIDWT, as shown in Fig. 8(a) and (b) when data are limited (the undersampling rate is lower than 35%). The improvement of reconstruction is more pronounced in Fig. 8(a) than in 8(b) for the proposed method. The reason may lie in that GBRWT makes use of smoothness more efficiently, because the corresponding source image in Fig. 5(a) is smoother than the latter.

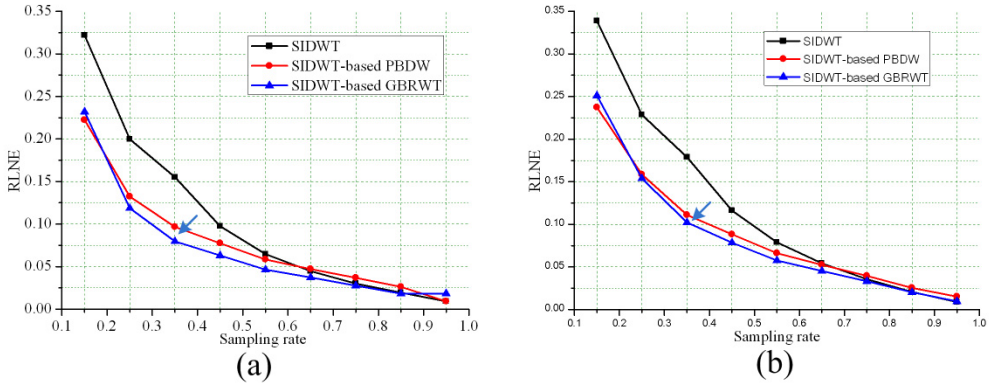

Fig. 8 RLNEs change with undersampling rate. The reference image of PBDW and GBRWT is the same SIDWT-based reconstructed image. Source images of (a-b) are Fig. 5(a) and (f).

4.2. With added noise

To test the performance of the proposed reconstruction method in noisy conditions, we simulate noisy data by adding Gaussian white noises with variance $\sigma^2 = 0.02$ on real and imaginary parts of k-space data. The SIDWT-based reconstructed image is adopted to be the reference image both in PBDW-based and in GBRWT-based methods.

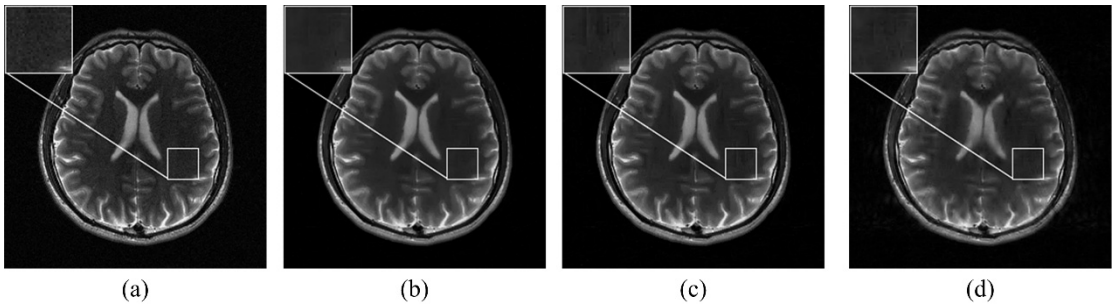

Fig. 9 Reconstructed images in noisy conditions. (a) the full sampled image with added noise; (b-d) reconstructed images using the proposed method, PBDW and SIDWT, respectively. The SNRs of (b-d) are 16.86, 14.97 and 14.06, respectively.

As shown in Fig. 9, GBRWT is observed to better suppress noises and artifacts than other methods. Noticeable noises exist in zoomed-in regions in reconstructed images based on SIDWT and PBDW visually. The SIDWT-based reconstructed image shows clear artifacts and

nearly loses the detail, and the reconstructed image using PBDW generates stripe-like artifacts as shown in the zoomed-in region in Fig. 9(c). The lowest reconstruction error is achieved using GBRWT, and the improvement of SNR is approximately 2dB. Therefore, GBRWT outperforms other methods when data are corrupted with noises.

4.3. Comparison with state-of-the-art methods

In this section, we compare the proposed method with dictionary learning MRI (DLMRI) (Ravishankar and Bresler, 2011), which is based on K-SVD decomposition, wavelet tree-structured MRI (WaTMRI) (Chen and Huang, 2014), which enforces the sparsity based on quadtree structures of wavelet coefficients, and PBDW (Qu et al., 2012), which is a patch-based directional wavelet transform that makes use of geometric information in patches. Default parameters of these methods are used in image reconstructions.

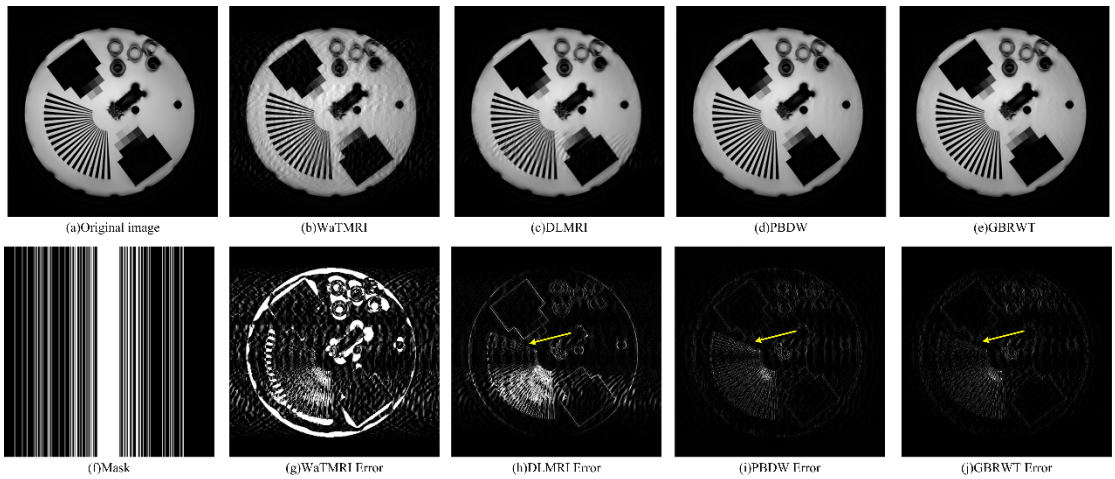

Fig. 10 Reconstructed images and errors in phantom experiment using Cartesian sampling with 27% data. (a) fullsampled image; (b-e) reconstructed images based on WaTMRI, DLMRI, PBDW and GBRWT respectively; (f) undersampling pattern;(g-j) reconstruction errors (scaled 5x).

Reconstructed images in Figs. 10 and 11 imply that the proposed method outperforms other methods in terms of removing aliasing artifacts as well as preserving edges. Reconstructed images in Fig. 10(b-d) show that the proposed method preserves edges much better than DLMRI and WaTMRI do. Remarkable improvements over PBDW are observed since image errors using PBDW are brighter than those of the proposed method. Zoomed-in

regions in Fig. 11(b, d-e) imply that aliasing artifacts using the new method have been better suppressed than those using other methods, and errors in Fig. 11(h) and (j) imply that the GBRWT has better edge preserving capabilities than DLMRI. Meanwhile, evaluation criteria listed in Table 2 imply superior performances of the proposed method, and remain the best in the tested dataset.

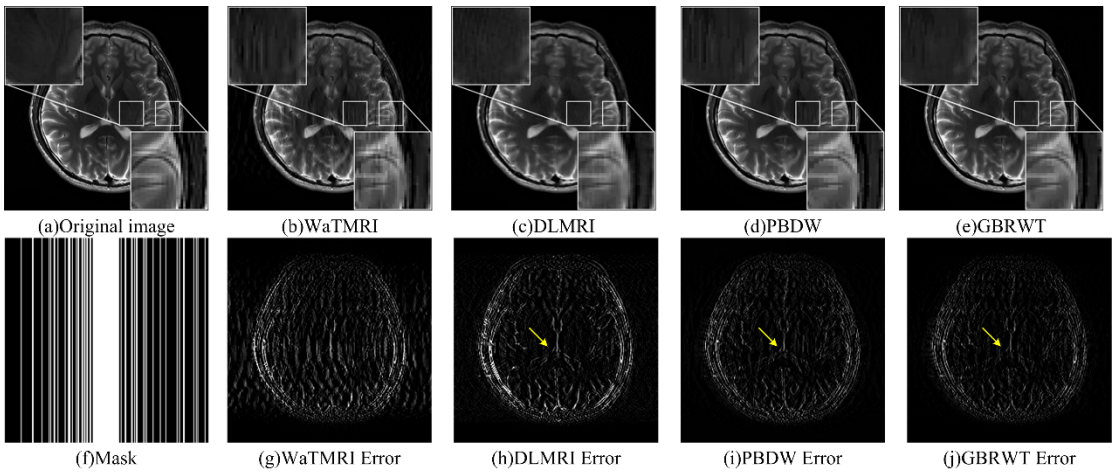

Fig. 11 Reconstructed images and errors using Cartesian sampling with 31% data. (a) full sampled image; (b-e) reconstructed images based on WaTMRI, DLMRI, PBDW and GBRWT respectively; (f) undersampling pattern; (g-j) reconstruction errors (scaled 5x).

Table 2 Comparison with the state-of-the-art methods when31% data are used in Cartesian sampling.

Images	WaTMRI			DLMRI			PBDW			GBRWT		
	SNR	MSSIM	RLNE	SNR	MSSIM	RLNE	SNR	MSSIM	RLNE	SNR	MSSIM	RLNE
Fig. 5(a)	12.59	0.8561	0.1424	14.27	0.8650	0.1414	17.12	0.9338	0.1012	**17.98**	**0.9527**	**0.0917**
Fig. 5(b)	15.23	0.8744	0.1119	17.24	0.8880	0.1053	19.52	0.9523	0.0807	**20.60**	**0.9683**	**0.0709**
Fig. 5(c)	8.26	0.7204	0.1822	18.04	0.8739	0.0820	20.99	0.9490	0.0592	**21.54**	**0.9593**	**0.0544**
Fig. 5(d)	9.20	0.6114	0.2567	17.79	0.8634	0.0955	19.26	0.9195	0.0806	**19.98**	**0.9315**	**0.0742**
Fig. 5(f)	13.06	0.8692	0.134	14.53	0.8650	0.1364	16.56	0.9331	0.1064	**17.59**	**0.9481**	**0.0943**

4.4. 2D Undersampling

In practice, 2D undersampling could be useful for 3D MR imaging when 2D phase encodings are available and 2D undersampling are applicable. However, we focus on 2D MR imaging in the present study. As the benefit of CS is usually seen in 2D undersampling, we implement 2D undersampling in simulation in this section. Reconstructed images in Figs. 12 and 13 imply that GBRWT preserves edges better than DLMRI, WaTMRI and PBDW when

pseudo radial sampling and 2D random undersampling are employed. Meanwhile, reconstructed errors of the proposed method with lowest brightness imply that GBRWT-based CS-MRI keep data fidelity best. Criteria listed in Tables 3 and 4indicate that the proposed method achieves highest SNRs and MSSIMs, and lowest RLNEs in the tested dataset. In summary, the proposed method performs better both in visual quality and reconstructed errors when 2D undersampling is implemented.

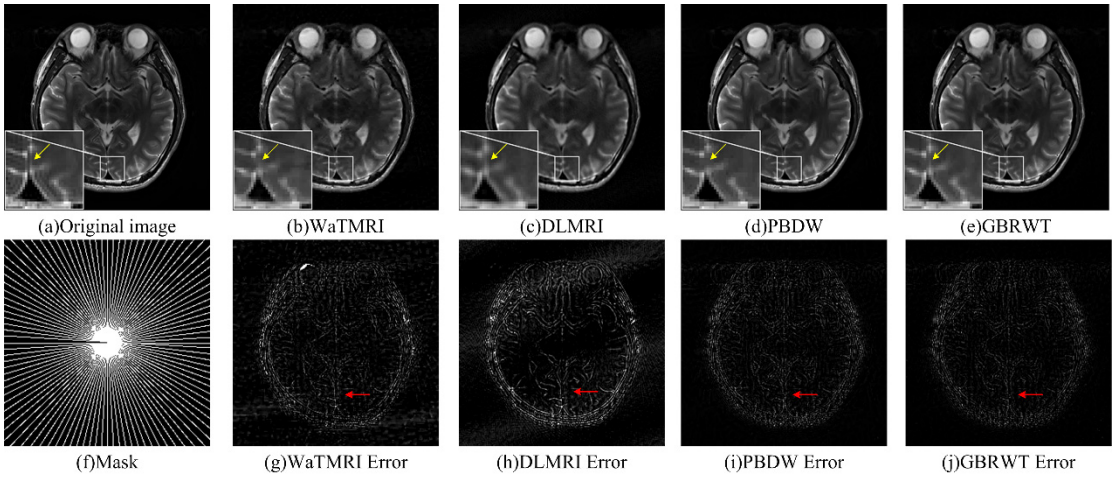

Fig. 12 Reconstructed images and errors with 22% data are used in pseudo radial sampling. (a) full sampled image; (b-e) reconstructed images based on WaTMRI, DLMRI, PBDW and GBRWT respectively; (f) undersampling pattern; (g-j) reconstruction errors (scaled 5x).

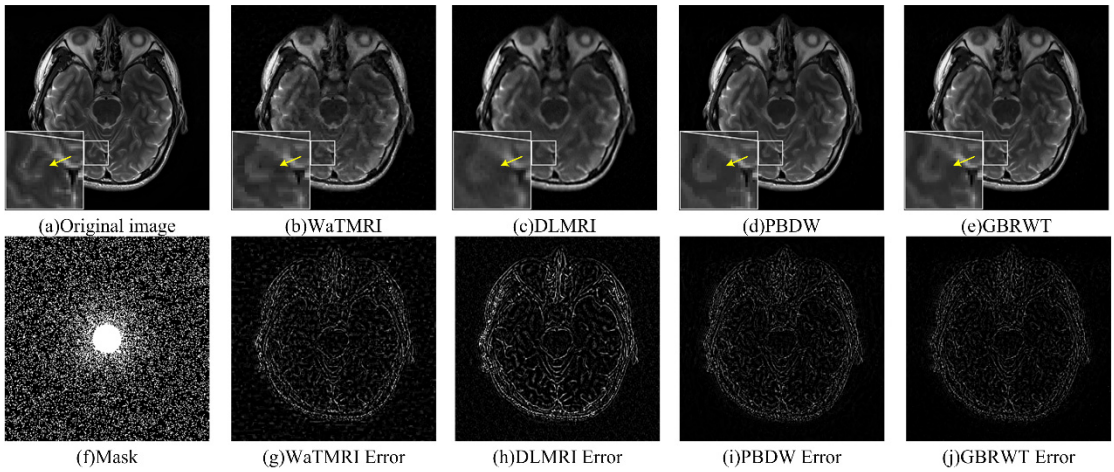

Fig. 13 Reconstructed images and errors with 20% data are used in 2D random sampling.(a) full sampled image; (b-e) reconstructed images based on WaTMRI, DLMRI, PBDW and GBRWT respectively; (f) undersampling pattern; (g-j) reconstruction errors (scaled 5x).

Table 3 Undersampling and reconstructionwhen 22% data are used in pseudo radial sampling.

Images	WaTMRI			DLMRI			PBDW			GBRWT		
	SNR	MSSIM	RLNE	SNR	MSSIM	RLNE	SNR	MSSIM	RLNE	SNR	MSSIM	RLNE
Fig. 5(e)	16.14	0.8609	0.1302	14.09	0.6949	0.1649	17.45	0.9122	0.1120	**18.24**	**0.9281**	**0.1023**
Fig. 5(f)	12.80	0.8452	0.139	12.27	0.6988	0.1737	16.09	0.9262	0.1151	**16.96**	**0.9406**	**0.1032**
Fig. 5(g)	12.93	0.8362	0.1286	13.02	0.7137	0.1583	17.27	0.9280	0.1002	**18.07**	**0.9408**	**0.0902**
Fig. 5(h)	14.15	0.8767	0.1112	13.51	0.6826	0.1523	18.76	0.9476	0.0860	**20.11**	**0.9638**	**0.0728**

Table 4 Undersampling and reconstruction when 20% data are used in 2D random sampling.

Images	WaTMRI			DLMRI			PBDW			GBRWT		
	SNR	MSSIM	RLNE	SNR	MSSIM	RLNE	SNR	MSSIM	RLNE	SNR	MSSIM	RLNE
Fig. 5(e)	13.16	0.8332	0.1444	13.01	0.7572	0.1693	15.85	0.8978	0.1211	**16.46**	**0.9109**	**0.1122**
Fig. 5(f)	12.45	0.8187	0.1485	12.38	0.7500	0.1744	15.59	0.9100	0.1195	**16.43**	**0.9205**	**0.1079**
Fig. 5(g)	12.43	0.8071	0.1426	13.08	0.7694	0.161	16.38	0.9086	0.1094	**17.21**	**0.9195**	**0.0985**
Fig. 5(h)	13.73	0.8509	0.1224	13.93	0.7823	0.1476	17.93	0.9360	0.0932	**19.44**	**0.9507**	**0.0773**

4.5. Effect of reference images

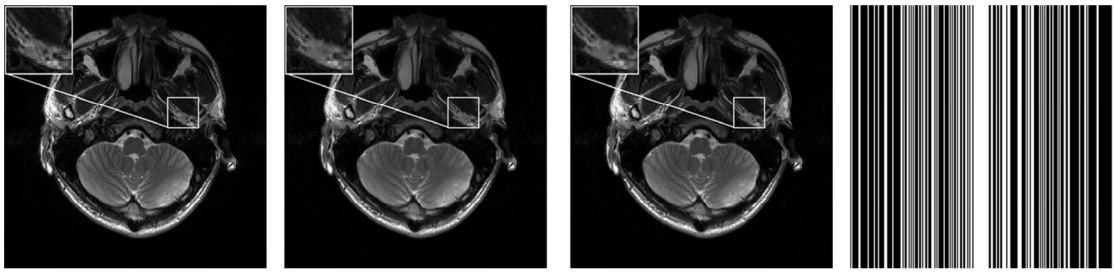

(a) (b) (c) (d)

Fig. 14 Reference images with better qualities cause better reconstructions. (a) is the full sampled image; (b-c) are reconstructed images using the SIDWT-based reconstructed and the full sampled image as references; (b-c) get RLNEs 0.109 and 0.095; (d) is the sampling pattern with undersampling rate 35%.

The GBRWT shows stronger abilities to retrieve the information from reference images. As shown in Fig. 14, when a fully sampled image is available, GBRWT can significantly reduce the reconstruction error than PBDW can. This fact implies GBRWT can learn more features

from a reference image than PBDW. In practice, GBRWT outperforms PBDW when no ground truth image can be used as reference images. However, the improvement of GBRWT over PBDW is less than that of learning from an optimal reference as shown in Fig. 15(a). Reasons may be the reduced resolution of reference image itself as well as the presence of artifacts in the SIDWT-based reconstructed images.

The GBRWT can follow PBDW-based reconstruction to further reduce reconstruction errors as shown in Fig. 15(b). The PBDW following GBRWT will improve the reconstruction, but its final reconstruction errors remain larger than those of GBRWT following PBDW. Therefore, using PBDW to generate the reference image is recommended. However, considering the computation time of PBDW, we recommend using SIDWT to reconstruct reference images since the improvement of using PBDW to achieve a reference is not significant as that of using SIDWT.

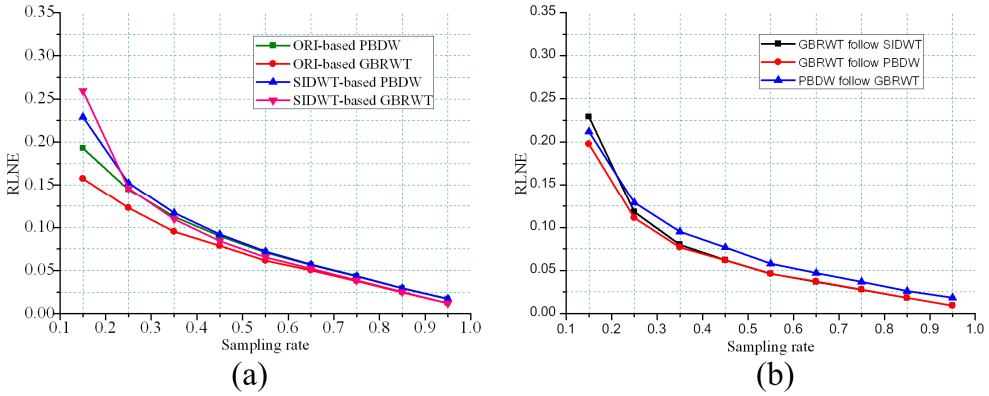

Fig. 15 Reconstruction errors when different reference images are used. (a) RLNE curves when the ground truth image and SIDWT-based reconstructed image are adopted as the reference image; (b) RLNE curves for GBRWT following PBDW or contrary.

4.6. Filters

While Haar filter is utilized as a typical setting in GBRWT, other filters are also considered. Figure 16 shows that comparable reconstructed images and errors will be obtained using different filters. This comparison implies that the proposed method is insensitive to selected filters. Therefore, Haar filter with simplicity and high speed is suggested.

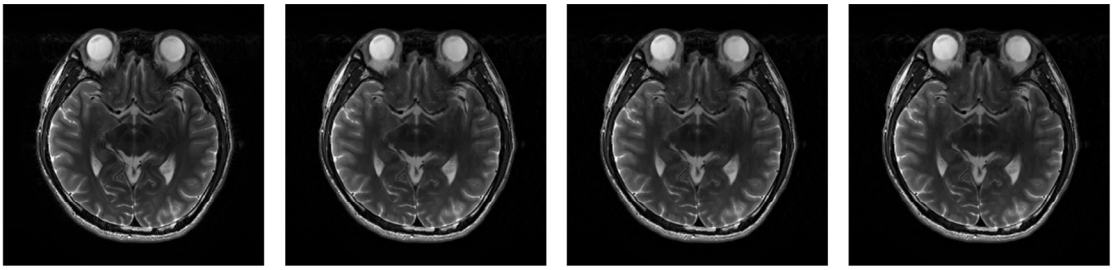

(a) (b) (c) (d)

Fig. 16 The GBRWT-based reconstructed images with different filters. (a) the full sampled image; (b-d) reconstructed images using filters: Haar, sym8 and db4. The RLNEs of (b-d) are 0.0935, 0.0943 and 0.0944 respectively.

4.7. Computation time

The GBRWT searches similar patches in a local region first, and expands its search to the whole region if no unvisited patches remain in local areas (Ram et al., 2011, 2012, 2013). This strategy reduces the computation time significantly in our implementation. The simulation performed on a four Intel Cores i7-2600 CPU at 3.4GHz and 16GB of our typical settings takes about 100s with twice optimization, which is not included 10 seconds for the first SIDWT-based reconstruction. Note that patch reordering induces in-1D filtering loop executions which are time consuming in nonparallel processes, but are valuable in finding accurate paths and increasing the redundancy.

5. Conclusion

In this article, a new image reconstruction method based on a graph-based redundant wavelet transform is proposed in CS-MRI. This method explores the graph structure to model images and images' approximate coefficients in each wavelet decomposition level to minimize the total difference of all image patches. Then the input signal can be smoothed by new orders estimated by solving travelling salesman problem in the graph. Wavelet filtering of smoother signals lead to sparser representations of magnetic resonance images, thus improve the reconstruction. Comparing with conventional shift-invariant wavelets and several state-of-the-art CS-MRI image reconstruction methods, including PBDW, DLMRI and WaTMRI, reconstructed images of proposed method are more consistent with fully sampled

images in image intensities and details. Further improvements can be obtained by optimizing permutation orders trained from the patch-based graph, further smoothing signals. Finally, parallel processes are expected to reduce the computation time caused by redundancy in future work.

Acknowledgments

The authors would like thank Drs. Bingwen Zheng, Feng Huang and Xi Peng for providing data in sections 3 and 4. The authors sincerely thank Drs. Michael Lustig, Junzhou Huang, Saiprasad Ravishankar and Yoram Bresler for sharing codes in the comparisons. The authors sincerely extend their appreciations to Professor Tim (Tien Mo) Shih for linguistic assistance. The authors are grateful to the reviewers for their thorough reviews. This work was supported by the NNSF of China (61201045, 11375147, 61302174), the Natural Science Foundation of Fujian Province of China (No. 2015J01346), Fundamental Research Funds for the Central Universities (2013SH002), and the Open Fund from the Key Lab of Digital Signal and Image Processing of Guangdong Province (2013GDDSIPL-07).

Reference

Aelterman, J., Luong, H.Q., Goossens, B., Pižurica, A., Philips, W., 2011. Augmented Lagrangian based reconstruction of non-uniformly sub-Nyquist sampled MRI data. Signal Processing 91, 2731-2742.

Aharon, M., Elad, M., Bruckstein, A., 2006. K-SVD: An algorithm for designing overcomplete dictionaries for sparse representation. IEEE Trans. Signal Process. 54, 4311-4322.

Akcakaya, M., Basha, T.A., Chan, R.H., Rayatzadeh, H., Kissinger, K.V., Goddu, B., Goepfert, L.A., Manning, W.J., Nezafat, R., 2012. Accelerated contrast-enhanced whole-heart coronary MRI using low-dimensional-structure self-learning and thresholding. Magn. Reson. Med. 67, 1434-1443.

Akcakaya, M., Basha, T.A., Goddu, B., Goepfert, L.A., Kissinger, K.V., Tarokh, V., Manning, W.J., Nezafat, R., 2011. Low-dimensional-structure self-learning and thresholding: regularization beyond compressed sensing for MRI reconstruction. Magn. Reson. Med. 66, 756-767.

Akcakaya, M., Basha, T.A., Pflugi, S., Foppa, M., Kissinger, K.V., Hauser, T.H., Nezafat, R., 2014. Localized spatio-temporal constraints for accelerated CMR perfusion. Magn. Reson. Med. 72, 629-639.

Baker, C.A., King, K., Dong, L., Leslie, Y., 2011. Translational-invariant dictionaries for compressed sensing in magnetic resonance imaging, 2011 IEEE International Symposium on Biomedical Imaging:

From Nano to Macro, 1602-1605.

Baraniuk, R., Choi, H., Neelamani, R., Ribeiro, V., Romberg, J., Guo, H., Fernandes, F., et.al, 2011. http://dsp.rice.edu/software/rice-wavelet-toolbox.

Chaari, L., Pesquet, J.C., Benazza-Benyahia, A., Ciuciu, P., 2011. A wavelet-based regularized reconstruction algorithm for SENSE parallel MRI with applications to neuroimaging. Med. Image Anal. 15, 185-201.

Chang, C.H., Ji, J., 2010. Improved compressed sensing MRI with multi-channel data using reweighted l(1) minimization, 2010 Annual International Conference Of the IEEE Engineering In Medicine And Biology Society, 875-878.

Chen, C., Huang, J.Z., 2014. The benefit of tree sparsity in accelerated MRI. Med. Image Anal. 18, 834-842.

Chen, Y.M., Ye, X.J., Huang, F., 2010. A novel method and fast algorithm for MR image reconstruction with significantly under-sampled data. Inverse Probl. Imaging 4, 223-240.

Cormen, T.H., Leiserson, C.E., Rivest, R.L., Stein, C., 2001. Introduction to algorithms. The MIT Press, Cambridge , Massachusetts London, England.

Daubechies, I., Defrise, M., De Mol, C., 2004. An iterative thresholding algorithm for linear inverse problems with a sparsity constraint. Commun. Pur. Appl. Math. 57, 1413-1457.

Greiser, A., von Kienlin, M., 2003. Efficient k-space sampling by density-weighted phase-encoding. Magn. Reson. Med. 50, 1266-1275.

Huang, F., Lin, W., Duensing, G.R., Reykowski, A., 2012. k-t sparse GROWL: Sequential combination of partially parallel imaging and compressed sensing in k-t space using flexible virtual coil. Magn. Reson. Med. 68, 772-782.

Jacob, M., 2009. Optimized non-uniform fast Fourier transform (NUFFT) for iterative tomographic reconstruction, 2009. 2009 IEEE International Conference on Acoustics, Speech and Signal Processing, 673-676.

Jim, J., Zhi-Pei, L., 2001. High resolution cardiac magnetic resonance imaging: a model-based approach, 2001. Proceedings of the 23rd Annual International Conference of the IEEE Engineering in Medicine and Biology Society, 2268-2271.

Junfeng, Y., Yin, Z., Wotao, Y., 2008. A fast TVL1-L2 minimization algorithm for signal reconstruction from partial Fourier data. CAAM 09-24, Rice university.

Junfeng, Y., Yin, Z., Wotao, Y., 2010. A fast alternating direction Method for TVL1-L2 signal reconstruction from partial fourier data. IEEE J. Sel. Top. Signal Process. 4, 288-297.

Khalidov, I., Fadili, J., Lazeyras, F., Van De Ville, D., Unser, M., 2011. Activelets: Wavelets for sparse representation of hemodynamic responses. Signal Processing 91, 2810-2821.

Lustig, M., Donoho, D.L., M.Santos, J., Pauly, J.M., 2008. Compressed sensing MRI. IEEE Signal Process. Mag. 72, 72-82.

Maggioni, M., Katkovnik, V., Egiazarian, K., Foi, A., 2013. Nonlocal transform-domain filter for volumetric data denoising and reconstruction. IEEE Trans. Image Process. 22, 119-133.

Majumdar, A., Ward, R.K., 2011. An algorithm for sparse MRI reconstruction by Schatten p-norm minimization. Magn. Reson. Imaging 29, 408-417.

Majumdar, A., Ward, R.K., 2012. Causal dynamic MRI reconstruction via nuclear norm minimization. Magn. Reson. Imaging 30, 1483-1494.

Majumdar, A., Ward, R.K., Aboulnasr, T., 2013. Non-convex algorithm for sparse and low-rank recovery: Application to dynamic MRI reconstruction. Magn. Reson. Imaging 31, 448-455.

Ning, B., Qu, X., Guo, D., Hu, C., Chen, Z., 2013. Magnetic resonance image reconstruction using trained geometric directions in 2D redundant wavelets domain and non-convex optimization. Magn. Reson. Imaging 31, 1611-1622.

Qu, X., Guo, D., Ning, B., Hou, Y., Lin, Y., Cai, S., Chen, Z., 2012. Undersampled MRI reconstruction with patch-based directional wavelets. Magn. Reson. Imaging 30, 964-977.

Qu, X., Hou, Y., Lam, F., Guo, D., Zhong, J., Chen, Z., 2014. Magnetic resonance image reconstruction from undersampled measurements using a patch-based nonlocal operator. Med. Image Anal. 18, 843-856.

Qu, X., Zhang, W., Guo, D., Cai, C., Cai, S., Chen, Z., 2010. Iterative thresholding compressed sensing MRI based on contourlet transform. Inverse Probl. Sci. En. 18, 737-758.

Ram, I., Elad, M., Cohen, I., 2011. Generalized tree-based wavelet transform. IEEE Trans. Signal Process. 59, 4199-4209.

Ram, I., Elad, M., Cohen, I., 2012. Redundant wavelets on graphs and high dimensional data clouds. IEEE Signal Process. Lett. 19, 291-294.

Ram, I., Elad, M., Cohen, I., 2013. Image processing using smooth ordering of its patches. IEEE Trans. Image Process. 22, 2764-2774.

Ravishankar, S., Bresler, Y., 2011. MR image reconstruction from highly undersampled k-space data by dictionary learning. IEEE Trans. Med. Imaging 30, 1028-1041.

Shensa, M., 1992. The discrete wavelet transform: wedding the a trous and Mallat algorithms. IEEE

Trans. Signal Process. 40, 2464-2482.

Singh, G., Raj, A., Kressler, B., Nguyen, T.D., Spincemaille, P., Zabih, R., Wang, Y., 2011. A fast edge-preserving bayesian reconstruction method for parallel imaging applications in cardiac MRI. Magn. Reson. Med.65, 184-189.

Skiena, S.S., 2008. The algorithm design manual. Springer, London.

Tsai, C.M., Nishimura, D.G., 2000. Reduced aliasing artifacts using variable-density k-space sampling trajectories. Magn. Reson. Med. 43, 452-458.

Wang, Y.-H., Qiao, J., Li, J.-B., Fu, P., Chu, S.-C., Roddick, J.F., 2014. Sparse representation-based MRI super-resolution reconstruction. Measurement 47, 946-953.

Wang, Y., Ying, L., 2014. Compressed sensing dynamic cardiac cine MRI using learned spatiotemporal dictionary. IEEE Trans. Biomed. Eng. 61, 1109-1120.

Weller, D.S., Polimeni, J.R., Grady, L., Wald, L.L., Adalsteinsson, E., Goyal, V.K., 2011. Combined compressed sensing and parallel mri compared for uniform and random cartesian undersampling of k-space, 2011 IEEE International Conference on Acoustics, Speech and Signal Processing (ICASSP), 553-556.

Weller, D.S., Polimeni, J.R., Grady, L., Wald, L.L., Adalsteinsson, E., Goyal, V.K., 2013. Sparsity-promoting calibration for GRAPPA accelerated parallel MRI reconstruction. IEEE Trans. Med. Imaging 32, 1325-1335.

Xiuquan, J., Jingfei, M., Aref, M., Wiener, E., Zhi-Pei, L., 2003. An improved MRI method for dynamic contrast-enhanced imaging of tumors, 2003. Proceedings of the 25th Annual International Conference of the IEEE Engineering in Medicine and Biology Society, 478-481.

Ying, D., Ji, J., 2011. Compressive sensing MRI with laplacian sparsifying transform, 2011 IEEE International Symposium on Biomedical Imaging: From Nano to Macro, 81-84.

Yue, H., Lingala, S.G., Jacob, M., 2012. A fast majorize-minimize algorithm for the recovery of sparse and low-rank matrices. IEEE Trans. Image Process. 21, 742-753.

Yue, H., Paisley, J., Qin, L., Xinghao, D., Xueyang, F., Xiao-Ping, Z., 2014. Bayesian nonparametric dictionary learning for compressed sensing MRI. IEEE Trans. Image Process. 23, 5007-5019.

Zhang, S.T., Zhan, Y.Q., Dewan, M., Huang, J.Z., Metaxas, D.N., Zhou, X.S., 2012. Towards robust and effective shape modeling: Sparse shape composition. Med. Image Anal. 16, 265-277.

Zhou, W., Bovik, A.C., Sheikh, H.R., Simoncelli, E.P., 2004. Image quality assessment: from error visibility to structural similarity. IEEE Trans. Image Process. 13, 600-612.